JGR Solid Earth

RESEARCH ARTICLE

Key Points:

- A high-resolution upper mantle deformation pattern was obtained by measuring XKS splitting parameters in Northeast China
- Generally, WNW-ESE oriented anisotropy is induced by asthenospheric return flow in the big mantle wedge convection
- The toroidal anisotropy reflects that the asthenospheric flow moved around the early stage foundering lithosphere beneath Songliao Basin

Subduction-Induced Asthenospheric Flow Around the Songliao Basin in NE China Revealed by Shear Wave Splitting Measurements of Dense Seismic Arrays

Tao Xu[1,2] [ID], **Yinshuang Ai[2,3,4]** [ID], **Chenglong Wu[1,2]**, **Ling Chen[2,4,5]** [ID], **Enbo Fan[3]**, **Long Li[3,4]**, and **Weiyu Dong[4,5]**

[1]Key Laboratory of Mineral Resources, Institute of Geology and Geophysics, Chinese Academy of Sciences, Beijing, China, [2]Innovation Academy for Earth Science, Chinese Academy of Sciences, Beijing, China, [3]Key Laboratory of Earth and Planetary Physics, Institute of Geology and Geophysics, Chinese Academy of Sciences, Beijing, China, [4]College of Earth and Planetary Sciences, University of Chinese Academy of Sciences, Beijing, China, [5]State Key Laboratory of Lithospheric Evolution, Institute of Geology and Geophysics, Chinese Academy of Sciences, Beijing, China

Abstract The traditional mantle plume model fails to explain late Cenozoic intraplate volcanism in Northeast China (NEC). We constrained the pattern of upper mantle deformation to study the origin of intraplate volcanism by quantifying the shear wave splitting parameters captured by three NW-SE linear seismic arrays in NEC. The dense station spacing (10 km) allowed us to image the small-scale variations in anisotropic structures in unprecedented detail. The WNW-ESE oriented subduction-parallel anisotropy is likely induced by the asthenospheric return flow in the big mantle wedge convection associated with Pacific subduction. Therein the most notable feature is a toroidal pattern of anisotropy beneath the Songliao Basin, which is distinguished by a larger splitting time (approximately 1.0 s) relative to weak anisotropy in the center. The toroidal anisotropy pattern coincides with a high-velocity anomaly extending from uppermost mantle down to ~300 km depth, presumably indicating early stage foundering lithosphere. The asthenospheric return flow then moved around the foundering lithosphere and induced the corresponding toroidal anisotropy. The decompression partial melting of upwelling asthenospheric materials erupted along weak zones generating late Cenozoic intraplate basalts on both flanks of the Songliao Basin. The high-density seismic array reveals that the Pacific subduction and early stage lithospheric foundering processes controlled the genesis of late Cenozoic volcanism in NEC.

Plain Language Summary Shear wave splitting analysis provides a direct and reliable approach to quantifying seismic azimuthal anisotropy and examine deformation in the lithosphere and upper asthenosphere, thus constraining mantle dynamics and tectonic processes. We present an upper mantle deformation pattern to study the genesis of intraplate volcanism in Northeast China by measuring shear wave splitting parameters. The small-scale variations in anisotropic structures were visualized in unprecedented detail thanks to dense station spacing (10 km). Generally the anisotropy pattern reflects the WNW-ESE oriented asthenospheric return flow in the big mantle wedge (BMW) convection associated with Pacific subduction. The toroidal anisotropy coincides with a remarkably high-velocity anomaly in the upper mantle beneath the Songliao Basin, indicating that the asthenospheric flow moved around the early stage foundering lithosphere. Decompression partial melting of upwelling asthenospheric materials created late Cenozoic intraplate basalts on both flanks of the Songliao Basin. This proposed geodynamic model provides a template for understanding lithosphere-asthenosphere interactions in BMW setting.

1. Introduction

When applied to plate boundaries such as midocean ridges and subduction zones, plate tectonics theory has satisfactorily explained the genesis of volcanism (Morgan, 1968). However, this hypothesis does not provide a satisfactory explanation for intraplate volcanism, which occurs far from plate boundaries (Lee & Grand, 2012). Intraplate volcanism is conventionally attributed to deep-rooted mantle plumes that originate at the core-mantle boundary (Morgan, 1971), such as the Hawaii volcanic chain, whereas the mantle plume model does not work for some intraplate volcanism. For instance, Cenozoic basaltic volcanism was widespread in Northeast China. The isotopic data indicate that the Northeast China volcanism was not caused by a high-^{3}He/^{4}He mantle plume (Chen et al., 2007). Moreover, the lower mantle does not exhibit slow seismic velocity anomaly at any depth

(Zhao et al., 2004). Hence, the plume hypothesis for Cenozoic volcanism in Northeast China does not have strong support.

When the Siberian craton and the North China craton collided and subducted, a composite fold belt known as Northeast China (NEC) was created (Şengör et al., 1993). Cenozoic volcanism occurred in NEC in an episodic way connected with the evolution of the Japan Sea and the concomitant geodynamic forcing of the India-Eurasia collision (Liu et al., 2001). Volcanic eruptions were confined to the Songliao Basin in the late Cretaceous before Japan Sea rifting. Volcanism then migrated into the lateral belts since ~29 Ma. The compressional stress caused by the opening of the Japan Sea probably resulted in weak volcanism during 29-16 Ma (Jolivet et al., 1994; Liu et al., 2001). The Songliao Basin's two flanks experienced the most intense volcanism following the end of the Japan Sea opening (Liu et al., 2001).

The origin and evolution of Cenozoic intraplate volcanism in NEC have been the subject of numerous geological studies, although the geodynamic mechanism is still debated. It is commonly accepted that magmatism is associated with the process of deep subduction of the Pacific plate, which has been seismically observed to be subhorizontally stationary in East Asia's MTZ (Huang & Zhao, 2006; Zhao et al., 2009). Lei and Zhao (2005) argued that the deep dehydration of the subducting slab and convective circulation of the big mantle wedge (BMW) result in large-scale upwelling of asthenospheric materials causing intraplate volcanism in Changbaishan. According to Tang et al. (2014), asthenospheric materials escaped through a crack in the subducting slab. Decompression melting, which is generated by upwelling, nourishes the Changbaishan volcanoes. Guo, Chen, et al. (2016) interpreted the Halaha and Abaga volcanoes as originating from regional asthenospheric upwelling induced by nearby downwelling, and this model was developed into a complex circulation pattern in the asthenosphere to explain other volcanism in NEC by surface wave dispersion, geoid height and surface heat flow inversion simultaneously (Zhang et al., 2022). Geochemical evidence supports a genetic relationship between deep subduction of the Pacific slab and Cenozoic intraplate volcanism in NEC despite distinct mechanisms (Kuritani et al., 2011; Sun et al., 2014, 2015; Xu et al., 2012; Zhang et al., 2015; Zhang & Guo, 2016; Zou et al., 2008). Moreover, numerical modeling indicates that intraplate magmatism was caused by Cenozoic interaction of the subducting Pacific slab with a hydrous mantle transition zone (Chen & Faccenda, 2019; Yang & Faccenda. 2020). Despite much work, it remains uncertain why late Cenozoic intraplate basalts were distributed surrounding the Songliao Basin, and within the basin, no volcanism has been detected since ~29 Ma (Liu et al., 2001). In particular, we need better constraints on the geodynamic process of deep subduction that caused late Cenozoic intraplate volcanism in NEC. Investigating the lateral variation in upper mantle deformation beneath NEC could aid in determining the genesis of late Cenozoic intraplate volcanism in the region.

The direction and amount of seismic azimuthal anisotropy can reveal crucial details regarding the deformation of lithosphere and asthenospheric flow (Silver & Chan, 1991). This anisotropy can be mapped through a study of shear wave splitting (SWS) in the teleseismic SKS, SKKS, and PKS phases (abbreviated XKS for convenience). A single shear wave may split into two orthogonal polarization-oriented shear waves as a result of seismic anisotropy. Splitting parameters include the fast shear wave polarization (φ) and the delay time between two waves (δt). These delineate the orientation of the anisotropic structure and the anisotropy magnitude, respectively. The lattice preferred orientation (LPO) of anisotropic minerals, primarily olivine, is usually thought to be the cause of seismic anisotropy in the upper mantle (Zhang & Karato, 1995). In the absence of high water content or partial melts the fast olivine crystallographic a axis has a tendency to line up with the finite-strain maximum-shear orientation under the condition of simple shear (Zhang & Karato, 1995). For a pure shear, the a axis would be consistent with the finite-strain extension orientation (Nicolas et al., 1973). In the scenario of simple mantle flow, the fast direction is usually interpreted as the flow direction (Silver, 1996).

Many studies have investigated seismic anisotropy beneath NEC and neighboring regions using shear wave splitting analysis, and the factors inducing anisotropy generally fall into three categories: lithospheric extension (Chen, Niu, Obayashi, et al., 2017; Li & Niu, 2010; Qiang & Wu, 2015), complex asthenospheric flow associated with subduction of the Pacific plate (Huang et al., 2011; Li et al., 2017; Lu et al., 2019, 2020; Yang et al., 2022) and the LPO of metastable olivine in the MTZ (Liu et al., 2008). This study interpreted three NW-SE oriented seismic profiles collected with relatively denser station spacing to investigate the anisotropy beneath NEC in detail (Figure 1). To ensure the reliability of the measurements, we corrected the sensor orientations before the SWS analysis. Furthermore, we used a spatial coherency method to determine the anisotropy depth (Gao & Liu, 2012; Liu & Gao, 2011) which enabled a more accurate interpretation of the SWS observations. Combined
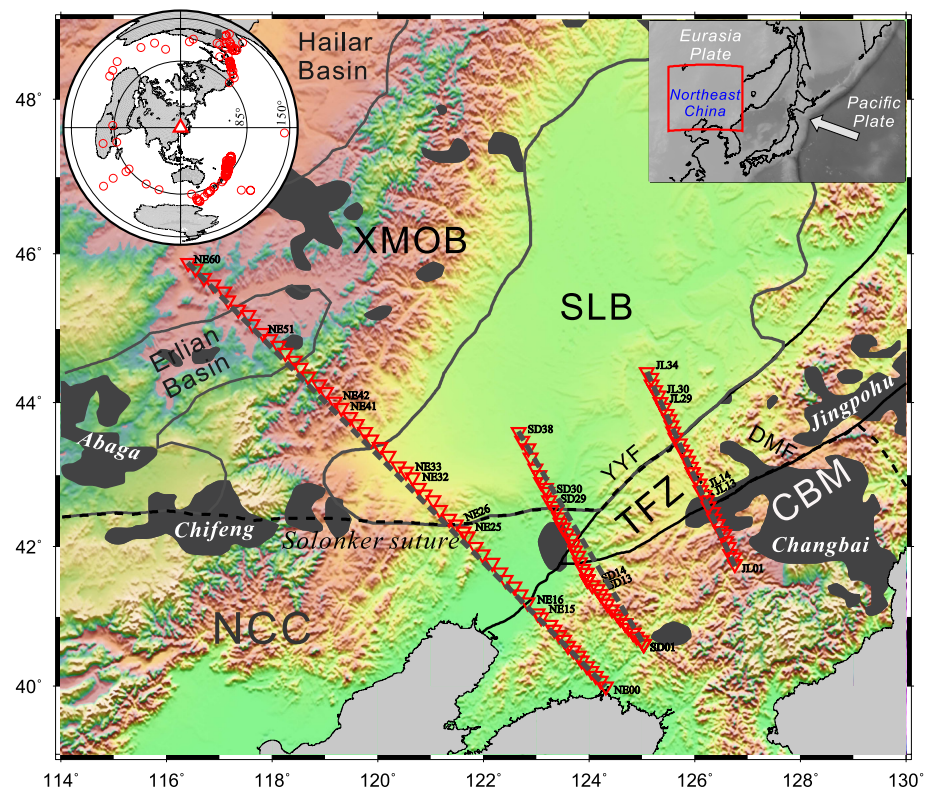
Figure 1. Major faults and tectonic units in Northeast China. The three NW-SE seismic profiles used in this study, from south to north, are NCISP6, NCISP10, and NCISP11 (shown as unfilled red triangles denoting stations). Some stations are marked with their station codes for reference. The major basins, the Songliao, Erlian, and Hailar Basins, are outlined by the gray solid lines. The Solonker suture is shown with a dashed line. Abbreviations: CBM, Changbaishan Mountain; TFZ, Tanlu fault zone; DMF, Dunhua-Mishan fault; YYF, Yilan-Yitong fault; SLB, Songliao Basin; XMOB, Xingmeng orogenic belt; NCC, North China craton. Late Cenozoic volcanism in Northeast China (NEC) is shown by the dark gray tone. In the top right inset, a red rectangle delineates the study area. The motion of the Pacific plate relative to the Eurasia plate is indicated by the arrow. The top left inset shows teleseismic events (red circles) used for XKS splitting analysis within 85° and 150° epicentral distances from the research zone.

with previous seismic tomography results and geochemical and geochronological evidence, the SWS measurements provide new constraints on geodynamic processes inducing late Cenozoic intraplate volcanism in NEC.

2. Data and Methods

2.1. Seismic Data Sources

Three NW-SE oriented linear seismic profiles captured the teleseismic data utilized in this study. The longest profile, referred to as NCISP6, contains 60 broadband stations spaced 10–17 km across the northern NCC and southern NEC and spanning 920 km from the Sino-North Korean border to the Sino-Mongolian border (Zheng et al., 2015). The stations were installed and operated from September 2007 to September 2008. The other two profiles, NCISP10 and NCISP11, consisted of 38 stations and 34 stations, respectively. The average station spacing was approximately 10 km. They both run from the Changbaishan mountain area to the Songliao Basin. The NCISP10 stations were deployed temporarily between October 2016 and July 2018, while the NCISP11 stations were deployed from August 2018 to December 2019.

### 2.2. Seismic Sensor Orientation Correction

The two horizontal components' real orientation relative to geographic north exerts a strong influence on particle motion measurements of XKS arrivals and fast direction. The orientation of the two horizontal components was determined by Wang et al. (2016) and Niu and Li (2011) by analysis of particle movements of teleseismic
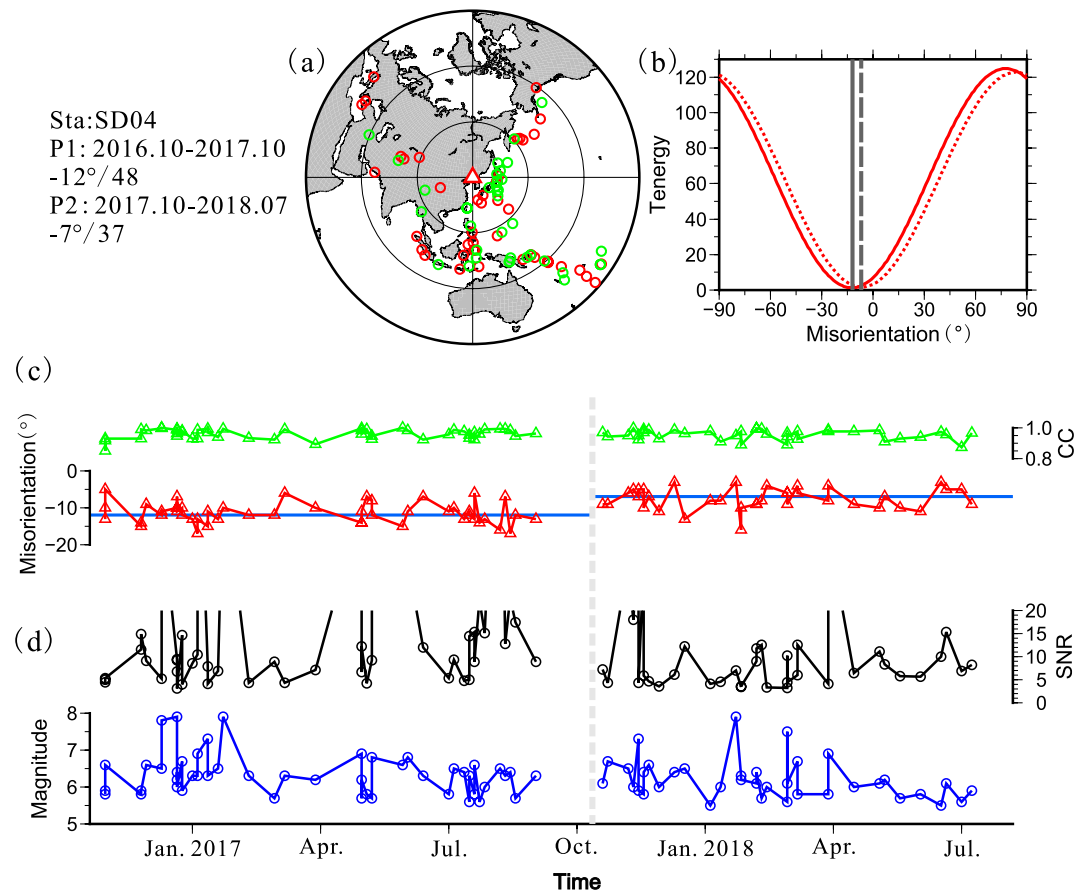
Figure 2. An application of the min*T* approach to data collected from station SD04. The record period is divided into two periods by the date of the sensor reinstallation (due to sensor failure). The period P1 was from October 2016 to October 2017 with a misorientation angle of −12° estimated from 48 events and a misorientation angle of −7° estimated from 37 events from the later period P2 (October 2017 to July 2018). (a) Earthquake distribution in the analysis. The red and green circles represent events analyzed by P1 and P2, respectively. (b) The red solid curve represents the sum of SNR-weighted normalized transverse energy (Tenergy) variation with misorientation angle of P1. The gray solid line points to the misorientation angle corresponding to the minimum Tenergy of P1. The dashed red curve and dashed gray line denote results obtained from P2 data. (c) The red triangles represent the single-earthquake min*T* measurements sorted by date with earthquake magnitude and SNR shown in the lower panel (d). The corresponding green triangles represent the cross coefficients of the vertical and radial components. After correcting for misorientation, these should approach one. The dashed gray line in (c, d) represents the date of sensor reinstallation. Prior to that date, misorientation angles are approximately −12° (shown as a blue line in P1), and after that date, the measurements are approximately −7° in P2.

P waves. We applied this technique to inspect and correct sensor misorientation prior to SWS analysis. We selected earthquakes with epicentral distances of 5°–90° and magnitudes of 5.5 or higher. After that, we used the long-period (5–50 s) teleseismic *P* waveforms as a basis for measuring sensor orientation applying the multiearthquake minimizing transverse energy (minT) approach. Figure 2 shows an example for station SD04. Due to sensor failure, the device was reinstalled in October 2017. This reduced the misorientation angle from −12° to −7° (in a clockwise direction from north). In addition to faulty installation, sensor misorientation can also arise from near-station structures. To account for all of these sources of error, Table S1 in Supporting Information S1 lists stations with azimuthal deviation ≥8° (Niu & Li, 2011). We assume that misorientation most likely arises from inadequate correction of magnetic declination, which is −9° in our study region. With only two stations having misorientation angles ≥8°, the NCISP6 array exhibited smaller misorientation angles relative to those of the other two arrays.

SWS analysis provides an effective means for demonstrating the sensor orientation correction accuracy. The results from transverse-component minimization (SC) and rotation-correlation (RC) approaches should agree well after sensor orientation correction (Tian et al., 2011; Wu et al., 2015). Sensor correction caused a clear decrease
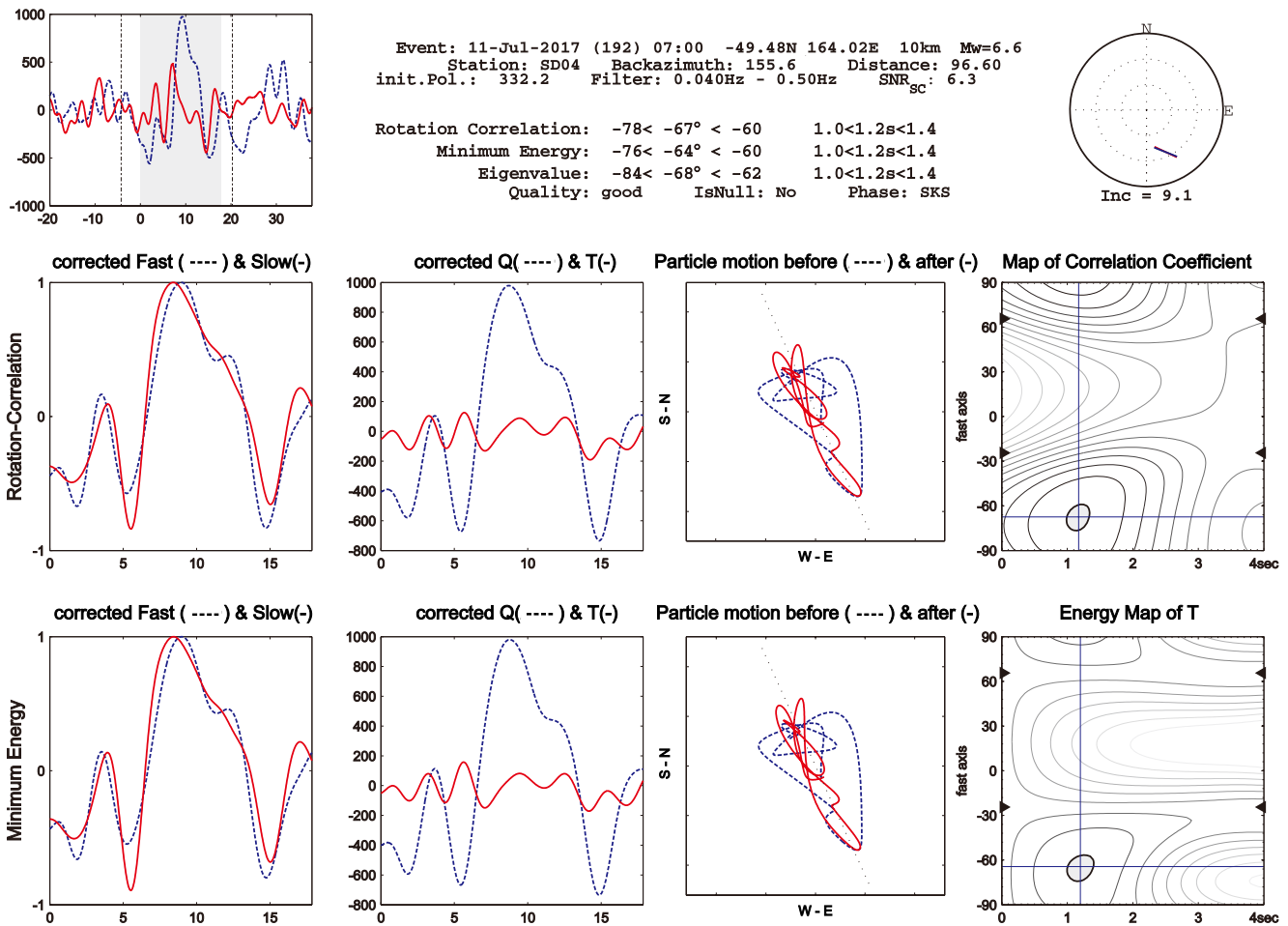
Figure 3. An illustration of Splitlab SWS Analysis (Wüstefeld et al., 2008) of the event 2019:192:07:00 recorded at station SD04 after misorientation correction. The original radial and transverse components are shown in the upper left panel represented by dashed and solid lines, respectively. The upper middle area lists the event and station information as well as the splitting information. A stereoplot with the station at its center is in the top right panel. Rotation-correlation (RC) and transverse-component minimization (SC) measurements are displayed in the middle and bottom panels, respectively. Left to right: fast and slow waveforms after correction, radial and transverse components after correction represented by Q and T, respectively, particle movement prior to and after correction and contour plot of various parameter pairings.

from 12° to 3° in the angular difference between the fast directions obtained by the SC and RC approaches (Figure 3 and Figure S1 in Supporting Information S1). For SC measurements, corrections also reconcile fast and slow waveforms and carry smaller measurement errors for splitting parameters.

2.3. XKS Splitting Measurements

Earthquakes with magnitudes of at least 5.5 and epicentral distances between 85° and 150° were chosen for SWS analysis. The study investigated 200 azimuthally well-covered events in total. They primarily occurred with NE and SW back azimuth angles. We employed SKS, SKKS, and PKS phases to quantify seismic anisotropy. Filtering seismic data with frequencies between 0.04 and 0.5 Hz, which covered the major XKS period, improved the signal-to-noise ratio.

SplitLab was used to determine the fast direction φ and delay time δt (Wüstefeld et al., 2008). We conducted a grid search for φ and δt by two methodologies, namely the rotation cross-correlation (RC) and transverse-component minimization (SC) (Bowman & Ando, 1987; Silver & Chan, 1991). The SC method looks for the minimum energy on the transverse component, while the RC technique seeks to maximize the cross-correlation coefficient for fast and slow waveforms. The theoretical XKS arrival times were calculated using IASP91 (Kennett et al., 1995). We measured splitting parameters over multiple time windows around XKS arrivals for each event to obtain
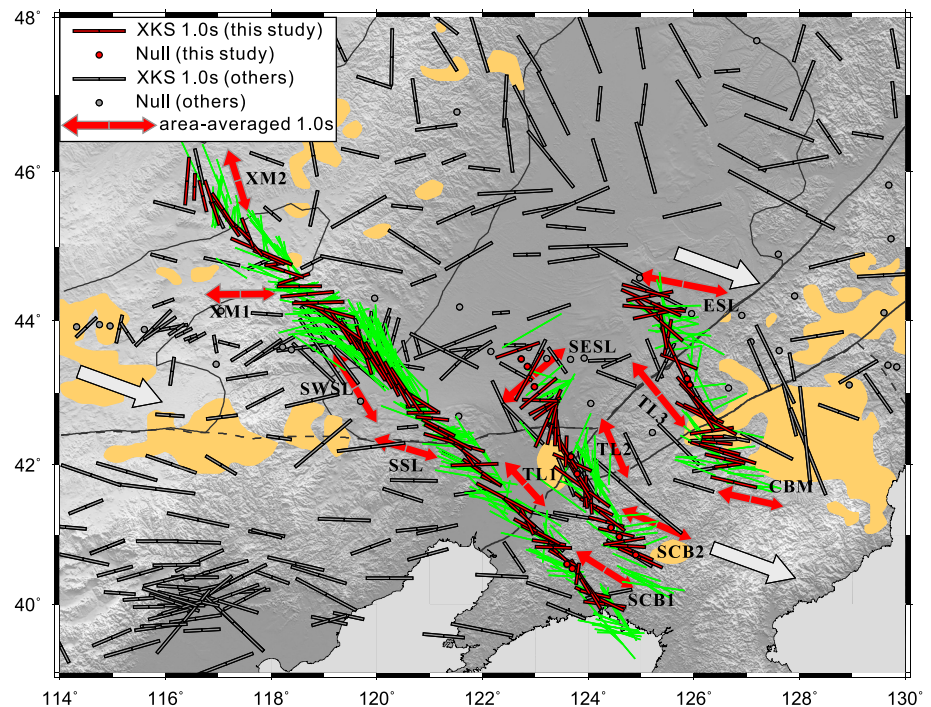
Figure 4. Station-averaged XKS results (dark red bars) compared to those reported by other research (gray bars; Li et al., 2017; Lu et al., 2019; Yang et al., 2022). Red and gray dots represent null measurements from the study and other studies, respectively. Green bars represent individual XKS results projected to piercing locations at a depth of 230 km. The red bidirectional arrows indicate the region-averaged XKS parameters from this study. The yellow color shows the late Cenozoic volcanism distribution in Northeast China (NEC). The white arrow indicates the asthenospheric return flow direction in the big mantle wedge.

robust results. The SC and RC approaches typically yield identical results for high-SNR events (see Figure 3). A comparison of the results generated by the two techniques enhanced the reliability of each splitting measurement and also distinguished null cases from viable splitting results (Wüstefeld & Bokelmann, 2007). If the wave travels across an isotropic medium or if the initial polarization corresponds with the fast or slow axis in a single layer with a horizontally symmetrical axis, the measurements are null (Savage, 1999; Silver & Chan, 1991).

Differentiations in the SC and RC results, including the angular difference in φ ($\Phi = |\varphi_{RC} - \varphi_{SC}|$) and the δt ratio ($\rho = \delta t_{RC}/\delta t_{SC}$) are used to assess the quality of the splitting results (Wüstefeld & Bokelmann, 2007). Conditions $\Phi \leq 10°$ and $0.8 \leq \rho \leq 1.1$, designate splitting measurements as "good" quality. Measurements with $\Phi \leq 15°$ and $0.7 \leq \rho \leq 1.2$ are categorized as "fair." The SNR for all measurements exceeded 3.0, and most error terms for φ and δt were less than 22.5° and 0.5 s, respectively. Manual selection of each event allowed us to remove the anisotropy effect typically through anisotropy correction with limited energy on the transverse component, coherent waveforms between fast and slow waveforms, and linearization of initially elliptical particle movement. The rigorous selection process improved the reliability of the splitting results. Measurements where $35° \leq \Phi \leq 55°$ and $\rho \leq 0.3$ were classified as null cases. Only splitting parameters generated by the SC method are described below because these exhibit stable behavior over a broader range of selected time windows. The RC results are considered for determining the quality rank.

3. Results

3.1. Spatial Variation in Splitting Parameters

Three NEC profiles including 130 stations provided a total of 278 well-defined splitting measurements categorized as "good" and "fair" and 694 null cases. We designated stations with splitting measurements as splitting stations and those with no splitting measurements and more than four null cases as null stations. Data from other stations were not analyzed due to scarce measurements. This yielded a total of 107 splitting stations and 12

null stations. Figure 4 shows the error-weighted station-averaged results for individual stations on a topographic map. Figures S2–S5 and Tables S2–S4 in Supporting Information S1 list the single-event and station-averaged results for each station. Measurement errors in station-averaged fast directions for five stations (NE17, SD32, JL13, JL15, and JL29) exceeded 35°, indicating a complex anisotropic structure beneath these stations. However, the limited quantity of splitting measurements from single stations makes it difficult to further investigate complicated cases. There is no systematic variation in splitting parameters or back azimuths for the other 102 splitting stations. This suggests that the observed SWS measurements can be attributed to a single anisotropic layer that possesses horizontal symmetry, not layered anisotropy as in North China or SE margin of Tibet (Gao et al., 2010, 2020). We therefore primarily focus on station-averaged results below.

The mean delay time (∼0.8 s) is less than the average value for continents of 1.0 s (Silver, 1996). The result agrees with values reported by previous studies of NEC (Chen, Niu, Obayashi, et al., 2017; Li et al., 2017; Li & Niu, 2010; Lu et al., 2019; Qiang & Wu, 2015; Zheng & Gao, 1994). To a first order, fast polarization directions show considerable variation. They are not consistent with the N110°E Absolute Plate Motion (APM) for NEC calculated by the GSRM V2.1 model (Kreemer et al., 2014), nor do they run parallel to primarily NE-oriented surface structures such as the Changbaishan Mountain or the Great Xing'an range. This suggests a complex origin for mantle anisotropy. Null stations occur in the southern part of the Songliao Basin, the Tanlu fault zone and in southern areas of the Changbaishan Mountain. The former cases were initially observed by Li et al. (2017).

Measurements were divided into 12 groups according to the location of the tectonic units and the characteristics of the splitting results (Figure 4 and Figure S6 in Supporting Information S1). Table S5 in Supporting Information S1 lists the group-averaged results. Splitting parameters for stations NE00-NE15, SD01-SD13, and JL01-JL13 in the Changbaishan Mountain region are referred to as group SCB1 (southern ChangBaishan Mountain), SCB2 and CBM, respectively. The fast directions mainly strike WNW-ESE. Stations NE16-NE25, SD14-SD29, and JL14-JL29 are located along the Tanlu fault zone, and are represented as groups TL1, TL2, and TL3, respectively. The fast directions strike NW-SE. Stations NE26-NE32, NE33-41, SD30-SD38, and JL30-JL34 occur in the southern Songliao Basin and belong to groups SSL (Southern Songliao Basin), SWSL (Southwestern Songliao Basin), SESL (Southeastern Songliao Basin), and ESL (Eastern Songliao Basin), respectively. Fast directions vary significantly for different groups. The mean results are NNW-SSE in SWSL, WNW-ESE in SSL, NE-SW in SESL, and WNW-ESE in ESL. These form a circular shape around the southern Songliao Basin. The largest splitting times of approximately 1.0 s in the SWSL, SESL, and SL groups occur in this area as well. The other two groups, XM1 and XM2 occur in the XMOB. These include stations NE52-NE51 and NE52-NE60, respectively. The mean fast directions shift from E-W in XM1 to NNW-SSE in XM2.

3.2. Comparison With Previous SWS Studies of NEC

There have been quite a few splitting parameters obtained from permanent and temporary stations around NEC. Some studies obtained results from the same stations. To facilitate the comparison, part of them is shown in Figure 4. The detailed comparison with previous SWS results is presented in Figures S8–S13 in Supporting Information S1. Using NECESSArray data collected by 127 stations that evenly covered most of NEC, Chen, Niu, Obayashi, et al. (2017) and Li et al. (2017) obtained roughly consistent results from most stations and distinct splitting parameters for several stations based on different selected events. Figure 4 shows the results from Li et al. (2017) compared with the SWS measurements from this study. Observations for stations near the SWSL, XM1, and XM2 groups are in good agreement with those made by Li et al. (2017) and the measurements of Yang et al. (2022), as well as those in Chen, Niu, Obayashi, et al. (2017) (Figure S9 in Supporting Information S1). They exhibit scattered fast directions that are aligned NW-SE, E-W, and NNW-SSE. Similarly, the stations along the western boundary of the southern Songliao Basin give large delay times (≥1.0 s). The fast directions for stations in ESL are oriented WNW-ESE, and consistent with the measurements in Li et al. (2017) and Chen, Niu, Obayashi, et al. (2017). The WNW-ESE aligned fast directions in SSL agree with those measured by Li et al. (2017) and Lu et al. (2019). However, the results in SESL and previous studies show scattered fast directions and lateral variation due to the complex upper mantle structure beneath the Songliao Basin. Stations located between 45°N and 46°N in the middle of the Songliao Basin give roughly E-W fast directions. When combined with the measurements from SWSL, SSL, SESL, and ESL in this study, observations form a toroidal pattern surrounding the southern Songliao Basin.

Lu et al. (2019) performed SWS analysis on data from permanent stations in the Changbaishan Mountain and Tanlu fault regions. They detected variations in fast axes from a WNW-ESE orientation in the Changbaishan
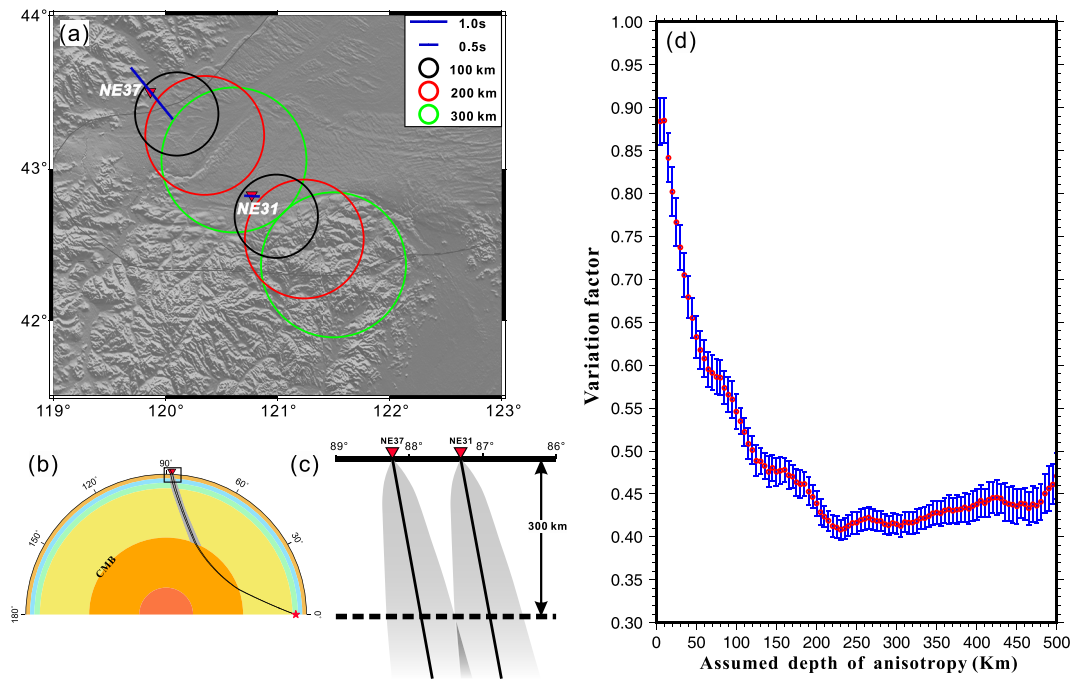
Figure 5. (a) Different Fresnel zones of SKS phases from event 2,007,289 at 100, 200, 300 km depths for station pair NE31 and NE37. (b) SKS paths of two earthquake-station pairs. The gray area denotes the Fresnel zones for the SKS paths. (c) The enlarged area denoted by the black rectangle in (b). The Fresnel zones for both branches merged below 300 km in depth. (d) Spatial coherency analysis based on XKS measurements to determine the anisotropy depth. Section 4.1 describes the procedure. Vertical bars denote uncertainties. The optimal estimate (minimum variation factor) indicates an anisotropy depth of approximately 230 km.

Mountain region to a NW-SE orientation in the Tanlu fault region. The present study detected a similar pattern in these regions, which also agree with the SWS observations made by Li and Niu (2010) in the Tanlu fault region.

4. Discussion

4.1. Estimating Anisotropy Depth Beneath the Study Area

Measurements of XKS splitting show a high level of lateral resolution but a low level of vertical resolution as a result of the steep XKS incidence. The depth of a horizontal anisotropy layer is often estimated using the intersecting Fresnel-zone method (Alsina & Snieder, 1995). The requirement that the Fresnel zones belonging to various splitting observations should not coincide places restrictions on the anisotropy depth. We calculated the Fresnel zones of event 2,007,289 at stations NE31 and NE37 (Figure 5a–5c). We chose the two stations due to the reliable observations and distinct splitting parameters. The approximate width of the Fresnel zone of SKS phases is determined by Width $= \sqrt{72L + 18}$, where L is the depth in km below the station (Hartog & Schwartz, 2000). The Fresnel zones of SKS for the station pair begin to overlap at approximately 300 km, suggesting that the primary source of anisotropy should be above the depth.

We used a more pervasive technique based on the spatial coherency of splitting parameters to determine more precise anisotropy depth (Gao & Liu, 2012). For a given assumed anisotropy depth, this procedure calculates a variation factor F_v that represents a weighted sum of the circular standard deviation (SD) of the fast direction and arithmetic SD of the delay time for overlapping blocks. When the splitting parameters are placed at the real anisotropy depth along the ray paths, the variation factor reaches a minimum to give the maximum spatial coherency of the splitting results. We searched for the best depth that corresponded to the smallest F_v within a range of 0–500 km at 5 km intervals. The success of this procedure depends on several factors (Liu & Gao, 2011). It is necessary to have a high-quality data set of individual splitting parameters measured from multiple events with sufficient azimuthal coverage. The second requirement is that the splitting parameters must exhibit a significant but smooth spatial variation. Finally, it assumes anisotropy in a single layer (Liu & Gao, 2011). Except for groups SWSL, XM1, and XM2, other groups have less than 25 measurements, and it is difficult to estimate the

anisotropy depth with the limited observations. The earthquake events used in SWSL came from northeast, southeast, and southwest quadrants, but the azimuthal coverage of events in XM1 and XM2 is not sufficient (Figure S7 in Supporting Information S1). Therefore, the procedure was applied in SWSL region. Figure 5d shows the resulting F_v curve. Beneath the southern Songliao Basin, the procedure indicates that a depth of 230 km generates the majority of the anisotropy. A recent S wave receiver function study from an ∼2,000 km E-W profile NECSaids has detected the lithosphere-asthenosphere boundary (LAB) west of the North-South Gravity Linement (NSGL) at ∼110–130 km, and the LAB east of the NSGL at ∼75–100 km (He et al., 2022), generally consistent with Meng et al. (2021) and Chen et al. (2008). Another SRF analysis from a 1,200 km-long profile north of the study region (Zhang et al., 2014) detected the LAB at a shallower depth of around 120 km beneath the northern Songliao and at ∼160 km on both east and west sides of the basin. We therefore conclude that the anisotropy beneath the southern Songliao included a major contribution from the upper asthenosphere. The limited number of measurements precluded estimation of the anisotropy depth beneath other regions. The anisotropy beneath most regions nevertheless appears to include a major contribution from the upper asthenosphere.

4.2. Anisotropic Pattern and Toroidal Asthenospheric Flow

The most intriguing feature in the data set presented here is distinct variations in splitting parameters in the southern Songliao Basin, which have also been detected by previous studies. Li and Niu (2010) reported variations from two stations along the western edge of the Songliao Basin. The study proposed that scattering observed in the fast direction may result from the interactions between edge-driven convection (Niu, 2005) caused by a step in the LAB and asthenospheric flow associated with the APM. Chen, Niu, Obayashi, et al. (2017) observed that splitting measurements exhibit large variations along the southwestern Songliao Basin. The study reported widespread lithospheric delamination beneath this study region. Li et al. (2017) obtained some null measurements in the southern Songliao Basin and interpreted them as evidence of downwelling flow triggered by mantle upwelling beneath the Changbaishan Mountain region. A denser set of XKS observations from the three NW-SE oriented profiles shows variation at a resolution necessary for distinguishing regional patterns. Along with previous studies, these show fast directions that form a toroidal pattern around the southern Songliao Basin. Figure 6a shows average fast directions and splitting times presented against a background S wave velocity model (Guo et al., 2018) for an anisotropic layer located at an approximately 230 km depth. This reveals that the toroidal fast directions and the high-velocity anomaly beneath the southern Songliao Basin are in good agreement. A first-order high-velocity anomaly can be seen in both horizontal slices and vertical profiles, and it extends from the top of the mantle to a depth of approximately 300 km (Guo et al., 2018; Figure S7 in Supporting Information S1). This feature appears in many previous studies using body or surface wave tomography (Guo, Chen, et al., 2016; Ma et al., 2018; Tang et al., 2014; Tao et al., 2018; Tian, Ma, et al., 2019; Figures S15 and S16 in Supporting Information S1). We infer that the high-velocity anomaly beneath the southern Songliao Basin probably represents foundering lithosphere.

The stations of XM1, SSL, and ESL, the stations at approximately 45°N (from Li et al., 2017) and CBM, SCB1 and SCB for the Changbaishan Mountain region give fast directions oriented WNW-ESE or E-W, which run roughly parallel to the APM. Along with the toroidal pattern of fast directions around the high-velocity anomaly, these results indicate that the WNW-ESE oriented asthenospheric flow encountered the foundering lithosphere and flowed around it toward the Changbaishan Mountain region (Figure 6a). Average splitting times exhibit features associated with the foundering lithosphere beneath the southern Songliao Basin. These change abruptly from ∼1.0 s outside the region to ∼0.5 s within the region (Figure 6b). The notable reduction in splitting time likely arises from a reorientation of the anisotropic geometry related to a localized shift from horizontal to vertical, supported by the negative radial anisotropy in the uppermost mantle beneath the southern Songliao Basin (Guo, Yang, & Chen, 2016) implying the lithospheric foundering process.

Except for the results in the Tanlu fault zone (Figure 7, discussed in Section 4.4), the parallelism between the APM of NEC and the direction of Pacific plate subduction suggests that two alternative processes could generate the WNW-ESE oriented anisotropy. They include (a) the rigid lithosphere of NEC floating upon the underlying asthenosphere and (b) the return flow of BMW convection caused by subduction (Faccenna et al., 2010). If the former process dominates, most observations in NEC should orient WNW-ESE, parallel to the APM. However, the fast directions shift from generally E-W at XM1 to N-S at XM2. Throughout NEC, fast directions shift from WNW-ESE south of ∼46° to NNW-SSE north of ∼46°. The orientations exhibit strong correlation with Pacific plate subduction geometry, which bends at the same latitude and shifts from roughly N-S to E-W in strike. We therefore interpret the return flow of BMW convection as the dominant asthenospheric flow pattern generating
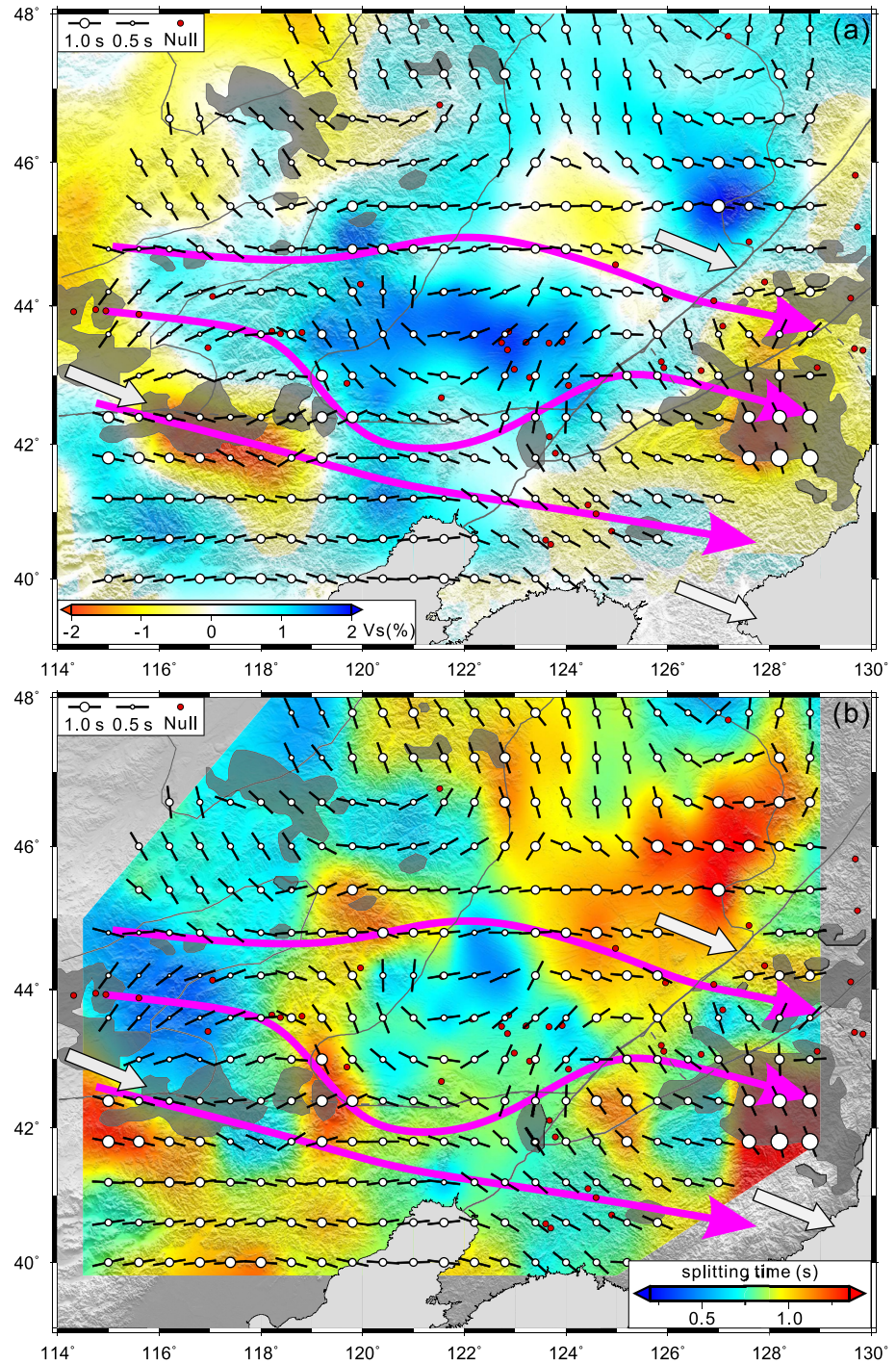
Figure 6. (a) Average splitting results are depicted on a shear-wave velocity model for a 230 km depth (Guo et al., 2018). The average fast directions and delay times are represented by the black bars and white circles, respectively. The circles are proportional to delay times. The average measurements taken with a 0.75°-radius are plotted on each 0.6° ⨯ 0.6° grid. Red dots represent the null case. The dark gray color represents the late Cenozoic volcanism distribution in Northeast China (NEC). The mantle flow direction is indicated by the purple arrows. The white arrow represents the direction of asthenospheric return flow in the big mantle wedge. (b) The lateral variation in the average delay time is depicted by a color contour map. Other symbols are the same as those in (a).
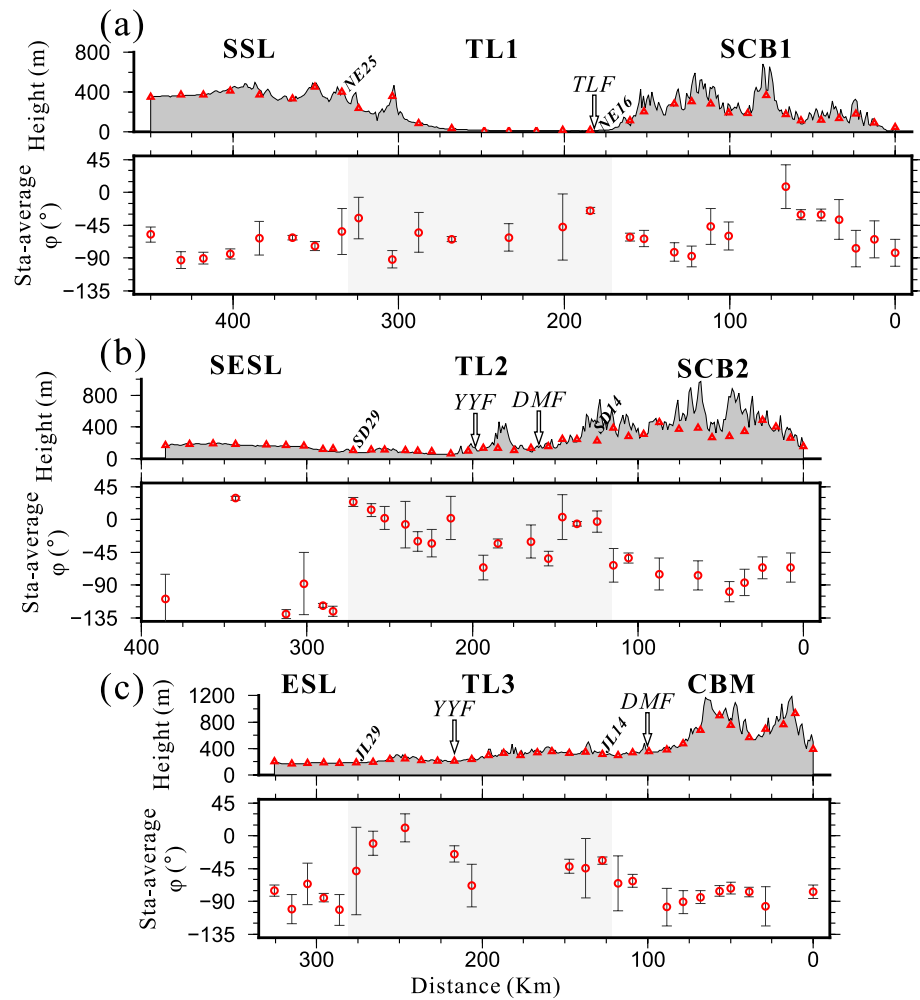
Figure 7. (a) The top panel shows the station locations (red triangles) for the NCISP6 profile projected to the line connecting stations NE00 and NE60 (dashed gray line in Figure 1). The horizontal axis indicates the distance from station NE00. The region codes, reference station codes, and faults are marked in the panel. The panel below denotes station-averaged fast directions with error. The gray area represents the Tanlu fault zone. (b) The top panel presents the NCISP10 station locations (red triangles) projected to the line connecting stations SD01 and SD38. The horizontal axis indicates the distance from station SD01. The other legends are the same as in (a). (c) The top panel presents the NCISP11 station locations (red triangles) projected to the line connecting stations JL01 and JL38. The horizontal axis indicates the distance from station JL01. The other legends are the same as in (a).

the observed anisotropy. From the perspective of geochemistry, the most plausible source of elevated $^{206}Pb/^{204}Pb$ components in partial NEC intraplate basalts is the deeply subducted Pacific slab because modern subducting sediments have remarkable radiogenic $^{206}Pb/^{204}Pb$, and lead isotopes in deeply subducted Pacific oceanic crust are identical to those found in Indian MORB (Xu, 2014). The relative contributions of deeply subducted Pacific materials grow progressively from Changbai to Abaga, which seems to contradict normal subduction polarity (Zhang & Guo, 2016). A *P* wave tomographic study by Ma et al. (2018) found that the Pacific plate extends west of the southern Songliao Basin and stagnates in the MTZ. As a result, we speculate that rapid mantle convection brought up the subducted Pacific elements along the slab's lateral edges (Faccenna et al., 2010), and subsequent decompression melting led to high $^{206}Pb/^{204}Pb$ of Abaga basalts. Then the return flow moved eastward and caused the gradual reduction in $^{206}Pb/^{204}Pb$ of the Chifeng and Changbai basalts.

4.3. A Geodynamic Model Linked to Late Cenozoic Intraplate Volcanism

The evolution of the Japan Sea back-arc basin is directly tied to Cenozoic volcanic episodes and stepwise propagation of volcanism in NEC (Liu et al., 2001). During the early stage (early Cenozoic ~29 Ma) prior to rifting of
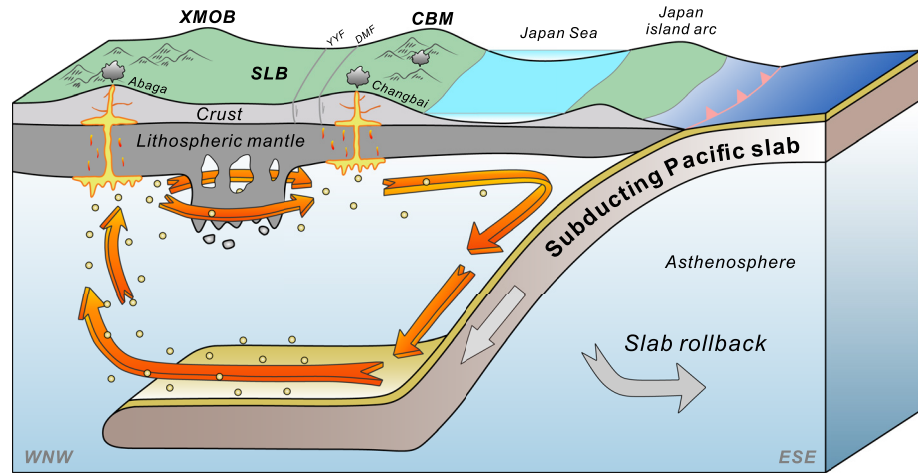
Figure 8. Interpretive sketch of the Cenozoic magmatic process in Northeast China (NEC). The asthenospheric return flow in the large mantle wedge (BMW), which was caused by the subducting Pacific slab, is indicated by the orange-red arrows. The direction of the Pacific slab's motion is shown by the gray arrow. The small yellow circles represent recycled oceanic crustal materials. The acronyms are the same as those given in the caption for Figure 1. The return flow moved around the early stage foundering lithosphere. The decompression partial melting of upwelling asthenospheric materials erupted along weak zones under lateral extension producing late Cenozoic intraplate basalts on both sides of the Songliao Basin.

the Japan Sea, volcanism was confined in the Songliao Basin, for example, the Eocene volcanism in Shuangliao (Xu et al., 2012). Young subducted oceanic crust (SOC), which was present in the basalt source, is thought to be responsible for the geochemical features of the Shuangliao Eocene basalts. The SOC components in basalts are generated from the stagnant Pacific slab in the MTZ beneath NEC (Xu et al., 2012). The opening of the Japan Sea occurred between 29 and 16 Ma as the western Pacific trench system migrated rapidly to the east (Jolivet et al., 1994; Yin, 2010). Coeval with the event, volcanism within the Songliao Basin as well as in NEC was greatly reduced or ceased, most likely as a result of the compressional stress caused by the Japan Sea's spreading in NEC. Structural analysis confirmed that the Bohai Bay Basin and nearby regions experienced a strong compressional event in the late Paleogene (Shi et al., 1999; Zhan & Zhu, 2012). Consequently, the lithosphere beneath the Songliao Basin gradually became thicker.

The high-velocity anomaly beneath the Songliao Basin presumably indicates a mantle lithospheric foundering process, which can be caused by delamination (Bird, 1979) or viscous downwelling resulting from Rayleigh-Taylor (RT) instability of cold and negatively buoyant lithosphere (Conrad & Molnar, 1997). Material descending as vertical drips aligns more with the expectations of an RT-type convective instability than with those of lithospheric delamination, which would predict material peeling away. The absence of mantle-sourced magmatism and the low topography of the Songliao Basin indicate that the foundering process is still at an early age. This is supported by the migrated S-RF profile which shows that the LAB beneath the Songliao Basin is not smooth and that several negative signals appear under the LAB (Figure 2b in He et al., 2022), suggesting that the majority of the foundering lithospheric material adheres to the lowermost lithosphere (Figure 8). After the Japan Sea opening ceased (16 Ma ~ present), the Songliao Basin experienced intense volcanic eruptions on both sides (Liu et al., 2001). The deep subducted Pacific slab induced convection in the BMW, which drove asthenospheric materials to upwell along the slab edge and return flow beneath NEC. The return flow encountered the foundering lithosphere beneath the Songliao Basin and flowed around it eastward. Under lateral extension following cessation of the Japan Sea opening, upwelling asthenospheric materials partially melted due to decompression and erupted along weak zones, inducing intraplate magmatism and volcanism in Abaga, Chifeng and Changbaishan (Figure 8). This scenario is supported by a geodynamic modeling study that reveals that magmatism begins at the margins of the instability and migrates inside in an RT-type instability (Wang & Currie, 2015).

Removal of the mantle lithosphere has been reported extensively in other global localities, such as the North China Craton (Chen, 2010; Chen et al., 2014), western US (Jiang et al., 2018; Yu et al., 2020), western Canada (Bao et al., 2014), central Tibet (Chen, Niu, Tromp, et al., 2017), and Antarctica (Shen et al., 2018). However, few studies have reported early stage lithosphere foundering. One example is that under eastern Tibet, an extremely

ancient and frigid Tibetan mantle layer is experiencing foundering (Bao & Shen, 2020). Another example is ongoing delamination-style lithospheric downwelling, which induces continuing Colorado Plateau uplift (Levander et al., 2011). The detailed anisotropic structure in NEC together with multidisciplinary measurements provide some of the best restrictions on the early stage lithosphere foundering process.

4.4. The Anisotropy of the Tanlu Fault Zone

Anisotropy beneath the southern NEC records asthenospheric return flow in the BMW. Most of the measurements tend to align in a WNW-ESE orientation parallel to Pacific plate subduction. However, fast directions within the Tanlu fault zone systematically shift to NW-SE along with some null measurements (Figure 7). Contrasts between NW-SE oriented fast directions and the WNW-ESE oriented Pacific plate subduction direction make it difficult to reconcile the anisotropy completely with the asthenospheric flow model. An alternative interpretation is that the anisotropy originates from lithospheric deformation. Extension was pervasive in Northeast China during the late Mesozoic and Cenozoic (Ren et al., 2002). Especially in the Early Cretaceous, NEC became a NW-SE extensional setting likely caused by retreat of the paleo-Pacific plate (Meng, 2003; Ren et al., 2002; Wilde, 2015; Wu et al., 2005). Since the Cretaceous, the DMF and the Huahui Basin that lies along the DMF in the Tanlu fault zone have experienced multistage contraction and extension (Huang et al., 2015; Liu et al., 2018). Extensional or rift tectonic environments generate horizontal foliation planes with stretching lineation parallel to the direction of extension. The NW-SE oriented anisotropy described here for the Tanlu fault zone is thus consistent with extensional deformation being frozen in the lithosphere since the late Mesozoic.

The crustal structural fabrics detected by receiver function imaging of NCISP6 data revealed the presence of a shallow Moho discontinuity as well as a Moho offset underneath the Tanlu fault zone (Zheng et al., 2015). Receiver function analysis of a large NEC data set detected clear Moho offsets across the YYF and DMF (Zhang et al., 2020). A deep seismic study across the Tanlu fault zone revealed that both the YYF and DMF penetrate the crust into the upper mantle with the Moho offset (Xu et al., 2017). Additionally, a magnetotelluric transect across the Tanlu fault zone detected a low-resistivity body clearly upwelling from the upper mantle to the upper crust beneath the YYF (Tian, Ye, et al., 2019). Collectively, the YYF and DMF in the Tanlu fault zone are most likely large deep faults that act as conduits for partially melted asthenospheric materials to upwell in an extensional setting. This likely causes the null measurements observed in the Tanlu fault zone (Figure 7).

5. Conclusion

To better understand the genesis of intraplate volcanism during the late Cenozoic in Northeast China, we measured the shear wave splitting of XKS phases from 130 stations of three NW-SE seismic profiles across NEC. Small-scale variation in anisotropy detected by dense station spacing indicates complex anisotropic features. The spatial coherency technique used here indicates that the anisotropic layer primarily resides in the upper asthenosphere. Numerous WNW-ESE subduction-parallel fast directions reflect that the anisotropy is dominated by the asthenospheric return flow in the BMW convection related to Pacific plate subduction. The anisotropy beneath the Songliao Basin exhibits a toroidal pattern in the fast direction. It corresponds with the high-velocity anomaly remaining in the upper mantle, presumably representing early stage lithospheric foundering. Subsequently by moving around the foundering lithosphere, the asthenospheric return flow induced the corresponding toroidal anisotropy. The decompression partial melting of upwelling asthenospheric materials erupted along weak zones under lateral extension. This dynamic process produced late Cenozoic intraplate basalts on both flanks of the southern Songliao Basin such as the Abaga, Chifeng and Changbaishan basalts. However, the anisotropy exhibits a systematic change in the Tanlu fault zone. The NW-SE aligned fast directions probably reflect lithospheric extension since the late Mesozoic. This suggests that the weak boundary zone has a considerable impact on lithospheric deformation and anisotropy in reaction to the long-term stress environment. The complicated deformation pattern of the study region indicates that the intraplate deformation may be controlled by the subduction process and associated strong lithosphere-asthenosphere interaction. The high-density seismic array reveals an ongoing lithospheric foundering process that may be responsible for the origin of late Cenozoic volcanism in NEC.

Data Availability Statement

The waveforms containing XKS phases of the portable stations in NCISP6, NCISP10, and NCISP11 are available at the WDC for Geophysics, Beijing (https://doi.org/10.12197/2022GA024).

References

Alsina, D., & Snieder, R. (1995). Small-scale sublithospheric continental mantle deformation: Constraints from SKS splitting observations. *Geophysical Journal International*, *123*(2), 431–448. https://doi.org/10.1111/j.1365-246x.1995.tb06864.x

Bao, X., Eaton, D. W., & Guest, B. (2014). Plateau uplift in Western Canada caused by lithospheric delamination along a craton edge. *Nature Geoscience*, *7*(11), 830–833. https://doi.org/10.1038/ngeo2270

Bao, X., & Shen, Y. (2020). Early-stage lithospheric foundering beneath the eastern Tibetan Plateau revealed by full-wave Pn tomography. *Geophysical Research Letters*, *47*, e2019GL086469. https://doi.org/10.1029/2019GL086469

Bird, P. (1979). Continental delamination and the Colorado plateau. *Journal of Geophysical Research*, *84*(B13), 7561–7571. https://doi.org/10.1029/JB084iB13p07561

Bowman, J. R., & Ando, M. (1987). Shear-wave splitting in the upper-mantle wedge above the Tonga subduction zone. *Geophysical Journal International*, *88*(1), 25–41. https://doi.org/10.1111/j.1365-246x.1987.tb01367.x

Chen, H., Niu, F., Obayashi, M., Grand, S. P., Kawakatsu, H., Chen, Y. J., et al. (2017). Mantle seismic anisotropy beneath NE China and implications for the lithospheric delamination hypothesis beneath the southern Great Xing'an range. *Earth and Planetary Science Letters*, *471*, 32–41. https://doi.org/10.1016/j.epsl.2017.04.030

Chen, L. (2010). Concordant structural variations from the surface to the base of the upper mantle in the North China Craton and its tectonic implications. *Lithos*, *120*(1–2), 96–115. https://doi.org/10.1016/j.lithos.2009.12.007

Chen, L., & Faccenda, M. (2019). Subduction-induced upwelling of a hydrous transition zone: Implications for the Cenozoic magmatism in northeast China. *Journal of Geophysical Research: Solid Earth*, *124*, 11489–11504. https://doi.org/10.1029/2019JB018133

Chen, L., Jiang, M., Yang, J., Wei, Z., Liu, C., & Ling, Y. (2014). Presence of an intralithospheric discontinuity in the central and Western North China Craton: Implications for destruction of the craton. *Geology*, *42*(3), 223–226. https://doi.org/10.1130/g35010.1

Chen, L., Tao, W., Zhao, L., & Zheng, T. (2008). Distinct lateral variation of lithospheric thickness in the Northeastern North China Craton. *Earth and Planetary Science Letters*, *267*(1–2), 56–68. https://doi.org/10.1016/j.epsl.2007.11.024

Chen, M., Niu, F., Tromp, J., Lenardic, A., Lee, C.-T. A., Cao, W., & Ribeiro, J. (2017). Lithospheric foundering and underthrusting imaged beneath Tibet. *Nature Communications*, *8*(1), 1–10. https://doi.org/10.1038/ncomms15659

Chen, Y., Zhang, Y., Graham, D., Su, S., & Deng, J. (2007). Geochemistry of Cenozoic basalts and mantle xenoliths in Northeast China. *Lithos*, *96*(1–2), 108–126. https://doi.org/10.1016/j.lithos.2006.09.015

Conrad, C. P., & Molnar, P. (1997). The growth of Rayleigh—Taylor-type instabilities in the lithosphere for various rheological and density structures. *Geophysical Journal International*, *129*(1), 95–112. https://doi.org/10.1111/j.1365-246x.1997.tb00939.x

Faccenna, C., Becker, T. W., Lallemand, S., Lagabrielle, Y., Funiciello, F., & Piromallo, C. (2010). Subduction-triggered magmatic pulses: A new class of plumes? *Earth and Planetary Science Letters*, *299*(1–2), 54–68. https://doi.org/10.1016/j.epsl.2010.08.012

Gao, S. S., & Liu, K. H. (2012). AnisDep: A FORTRAN program for the estimation of the depth of anisotropy using spatial coherency of shear-wave splitting parameters. *Computers & Geosciences*, *49*, 330–333. https://doi.org/10.1016/j.cageo.2012.01.020

Gao, Y., Shi, Y., & Wang, Q. (2020). Seismic anisotropy in the southeastern margin of the Tibetan Plateau and its deep tectonic significances. *Chinese Journal of Geophysics*, *63*(3), 802–816.

Gao, Y., Wu, J., Yi, G., & Shi, Y. (2010). Crust-mantle coupling in North China: Preliminary analysis from seismic anisotropy. *Chinese Science Bulletin*, *55*(31), 3599–3605. https://doi.org/10.1007/s11434-010-4135-y

Guo, Z., Chen, Y. J., Ning, J., Yang, Y., Afonso, J. C., & Tang, Y. (2016). Seismic evidence of on-going sublithosphere upper mantle convection for intra-plate volcanism in Northeast China. *Earth and Planetary Science Letters*, *433*, 31–43. https://doi.org/10.1016/j.epsl.2015.09.035

Guo, Z., Wang, K., Yang, Y., Tang, Y., John Chen, Y., & Hung, S. H. (2018). The origin and mantle dynamics of quaternary intraplate volcanism in Northeast China from joint inversion of surface wave and body wave. *Journal of Geophysical Research: Solid Earth*, *123*, 2410–2425. https://doi.org/10.1002/2017JB014948

Guo, Z., Yang, Y., & Chen, Y. J. (2016). Crustal radial anisotropy in Northeast China and its implications for the regional tectonic extension. *Geophysical Journal International*, *207*(1), 197–208. https://doi.org/10.1093/gji/ggw261

Hartog, R., & Schwartz, S. Y. (2000). Subduction-induced strain in the upper mantle east of the Mendocino Triple Junction, California. *Journal of Geophysical Research*, *105*(B4), 7909–7930. https://doi.org/10.1029/1999JB900422

He, Y., Chen, Q. F., Chen, L., Wang, X., Guo, G., Li, T., et al. (2022). Distinct lithospheric structure in the Xing'an-Mongolian orogenic belt. *Geophysical Research Letters*, *49*, e2021GL097283. https://doi.org/10.1029/2021GL097283

Huang, J., & Zhao, D. (2006). High-resolution mantle tomography of China and surrounding regions. *Journal of Geophysical Research*, *111*, B09305. https://doi.org/10.1029/2005JB004066

Huang, S., Dong, S., Zhang, Y., Zhang, F., Huang, D., Wei, S., et al. (2015). The deformation and tectonic evolution of the Huahui Basin, Northeast China, during the Cretaceous-early Cenozoic. *Journal of Asian Earth Sciences*, *114*, 717–731. https://doi.org/10.1016/j.jseaes.2015.05.013

Huang, Z., Wang, L., Zhao, D., Mi, N., & Xu, M. (2011). Seismic anisotropy and mantle dynamics beneath China. *Earth and Planetary Science Letters*, *306*(1–2), 105–117. https://doi.org/10.1016/j.epsl.2011.03.038

Jiang, C., Schmandt, B., Hansen, S. M., Dougherty, S. L., Clayton, R. W., Farrell, J., & Lin, F.-C. (2018). Rayleigh and S wave tomography constraints on subduction termination and lithospheric foundering in central California. *Earth and Planetary Science Letters*, *488*, 14–26. https://doi.org/10.1016/j.epsl.2018.02.009

Jolivet, L., Tamaki, K., & Fournier, M. (1994). Japan Sea, opening history and mechanism: A synthesis. *Journal of Geophysical Research*, *99*(B11), 22237–22259. https://doi.org/10.1029/93JB03463

Kennett, B. L., Engdahl, E., & Buland, R. (1995). Constraints on seismic velocities in the Earth from traveltimes. *Geophysical Journal International*, *122*(1), 108–124. https://doi.org/10.1111/j.1365-246x.1995.tb03540.x

Kreemer, C., Blewitt, G., & Klein, E. C. (2014). A geodetic Plate Motion and global strain rate model. *Geochemistry, Geophysics, Geosystems*, *15*, 3849–3889. https://doi.org/10.1002/2014GC005407

Kuritani, T., Ohtani, E., & Kimura, J.-I. (2011). Intensive hydration of the mantle transition zone beneath China caused by ancient slab stagnation. *Nature Geoscience*, *4*(10), 713–716. https://doi.org/10.1038/ngeo1250

Lee, C.-T. A., & Grand, S. P. (2012). Intraplate volcanism. *Nature*, *482*(7385), 314–315. https://doi.org/10.1038/482314a

Lei, J., & Zhao, D. (2005). P-wave tomography and origin of the Changbai intraplate volcano in Northeast Asia. *Tectonophysics*, *397*(3–4), 281–295. https://doi.org/10.1016/j.tecto.2004.12.009

Levander, A., Schmandt, B., Miller, M., Liu, K., Karlstrom, K., Crow, R., et al. (2011). Continuing Colorado plateau uplift by delamination-style convective lithospheric downwelling. *Nature*, *472*(7344), 461–465. https://doi.org/10.1038/nature10001

Li, J., & Niu, F. (2010). Seismic anisotropy and mantle flow beneath northeast China inferred from regional seismic networks. *Journal of Geophysical Research*, *115*, B12327. https://doi.org/10.1029/2010JB007470

Li, S., Guo, Z., & Chen, Y. J. (2017). Complicated 3D mantle flow beneath Northeast China from shear wave splitting and its implication for the Cenozoic intraplate volcanism. *Tectonophysics*, *709*, 1–8. https://doi.org/10.1016/j.tecto.2017.04.015

Liu, C., Zhu, G., Zhang, S., Gu, C., Li, Y., Su, N., & Xiao, S. (2018). Mesozoic strike-slip movement of the Dunhua-Mishan fault zone in NE China: A response to oceanic plate subduction. *Tectonophysics*, *723*, 201–222. https://doi.org/10.1016/j.tecto.2017.12.024

Liu, J., Han, J., & Fyfe, W. S. (2001). Cenozoic episodic volcanism and continental rifting in northeast China and possible link to Japan Sea development as revealed from K–Ar geochronology. *Tectonophysics*, *339*(3–4), 385–401. https://doi.org/10.1016/s0040-1951(01)00132-9

Liu, K. H., & Gao, S. S. (2011). Estimation of the depth of anisotropy using spatial coherency of shear-wave splitting parameters. *Bulletin of the Seismological Society of America*, *101*(5), 2153–2161. https://doi.org/10.1785/0120100258

Liu, K. H., Gao, S. S., Gao, Y., & Wu, J. (2008). Shear wave splitting and mantle flow associated with the deflected Pacific slab beneath northeast Asia. *Journal of Geophysical Research*, *113*, B01305. https://doi.org/10.1029/2007JB005178

Lu, M., Lei, J., & Zhang, G. (2019). Upper-mantle seismic anisotropy structure and dynamics beneath NE China inferred from SKS splitting analysis. *Chinese Journal of Geophysics*, *62*(9), 3365–3384.

Lu, M., Lei, J., Zhao, D., Ai, Y., Xu, X., & Zhang, G. (2020). SKS splitting measurements in NE China: New insights into the Wudalianchi intraplate volcanism and mantle dynamics. *Journal of Geophysical Research: Solid Earth*, *125*, e2019JB018575. https://doi.org/10.1029/2019JB018575

Ma, J., Tian, Y., Liu, C., Zhao, D., Feng, X., & Zhu, H. (2018). P-wave tomography of Northeast Asia: Constraints on the Western Pacific plate subduction and mantle dynamics. *Physics of the Earth and Planetary Interiors*, *274*, 105–126. https://doi.org/10.1016/j.pepi.2017.11.003

Meng, F., Ai, Y., Xu, T., Chen, L., Wang, X., & Li, L. (2021). Lithospheric structure beneath the boundary region of north China craton and Xing Meng orogenic belt from S-receiver function analysis. *Tectonophysics*, *818*, 229067. https://doi.org/10.1016/j.tecto.2021.229067

Meng, Q.-R. (2003). What drove late Mesozoic extension of the northern China-Mongolia tract? *Tectonophysics*, *369*(3–4), 155–174. https://doi.org/10.1016/s0040-1951(03)00195-1

Morgan, W. J. (1968). Rises, trenches, great faults, and crustal blocks. *Journal of Geophysical Research*, *73*(6), 1959–1982. https://doi.org/10.1029/JB073i006p01959

Morgan, W. J. (1971). Convection plumes in the lower mantle. *Nature*, *230*(5288), 42–43. https://doi.org/10.1038/230042a0

Nicolas, A., Boudier, F., & Boullier, A. (1973). Mechanisms of flow in naturally and experimentally deformed peridotites. *American Journal of Science*, *273*(10), 853–876. https://doi.org/10.2475/ajs.273.10.853

Niu, F., & Li, J. (2011). Component azimuths of the CEArray stations estimated from P-wave particle motion. *Earthquake Science*, *24*(1), 3–13. https://doi.org/10.1007/s11589-011-0764-8

Niu, Y. (2005). Generation and evolution of basaltic magmas: Some basic concepts and a new view on the origin of Mesozoic-Cenozoic basaltic volcanism in eastern China. *Geological Journal of China Universities*, *11*(1), 9–46.

Qiang, Z.-Y., & Wu, Q.-J. (2015). Upper mantle anisotropy beneath the north of northeast China and its dynamic significance. *Chinese Journal of Geophysics*, *58*(10), 3540–3552.

Ren, J., Tamaki, K., Li, S., & Zhang, J. (2002). Late Mesozoic and Cenozoic rifting and its dynamic setting in Eastern China and adjacent areas. *Tectonophysics*, *344*(3–4), 175–205. https://doi.org/10.1016/s0040-1951(01)00271-2

Savage, M. (1999). Seismic anisotropy and mantle deformation: What have we learned from shear wave splitting? *Reviews of Geophysics*, *37*(1), 65–106. https://doi.org/10.1029/98RG02075

Şengör, A., Natal, B., & Burtman, V. (1993). Evolution of the Altaid tectonic collage and Palaeozoic crustal growth in Eurasia. *Nature*, *364*(6435), 299–307. https://doi.org/10.1038/364299a0

Shen, W., Wiens, D. A., Stern, T., Anandakrishnan, S., Aster, R. C., Dalziel, I., et al. (2018). Seismic evidence for lithospheric foundering beneath the southern Transantarctic Mountains, Antarctica. *Geology*, *46*(1), 71–74. https://doi.org/10.1130/g39555.1

Shi, B., Wu, Z., Wang, J., Zhou, Y., & Dai, Q. (1999). A study on the geological characteristics and geodynamic origin of Dongying Movement, Bohai Bay Basin. *Petroleum Geology & Experiment*, *21*(3), 196–200.

Silver, P. G. (1996). Seismic anisotropy beneath the continents: Probing the depths of geology. *Annual Review of Earth and Planetary Sciences*, *24*(1), 385–432. https://doi.org/10.1146/annurev.earth.24.1.385

Silver, P. G., & Chan, W. W. (1991). Shear wave splitting and subcontinental mantle deformation. *Journal of Geophysical Research*, *96*(B10), 16429–16454. https://doi.org/10.1029/91JB00899

Sun, Y., Ying, J., Su, B., Zhou, X., & Shao, J. (2015). Contribution of crustal materials to the mantle sources of Xiaoguilhe ultrapotassic volcanic rocks, Northeast China: New constraints from mineral chemistry and oxygen isotopes of olivine. *Chemical Geology*, *405*, 10–18. https://doi.org/10.1016/j.chemgeo.2015.04.005

Sun, Y., Ying, J., Zhou, X., Chu, Z., & Su, B. (2014). Geochemistry of ultrapotassic volcanic rocks in Xiaoguilhe NE China: Implications for the role of ancient subducted sediments. *Lithos*, *208*, 53–66. https://doi.org/10.1016/j.lithos.2014.08.026

Tang, Y., Obayashi, M., Niu, F., Grand, S. P., Chen, Y. J., Kawakatsu, H., et al. (2014). Changbaishan volcanism in northeast China linked to subduction-induced mantle upwelling. *Nature Geoscience*, *7*(6), 470–475. https://doi.org/10.1038/ngeo2166

Tao, K., Grand, S. P., & Niu, F. (2018). Seismic structure of the upper mantle beneath eastern Asia from full waveform seismic tomography. *Geochemistry, Geophysics, Geosystems*, *19*, 2732–2763. https://doi.org/10.1029/2018GC007460

Tian, J., Ye, G., Ding, Z., Wu, Q., Wei, W., Jin, S., & Xie, C. (2019). A study of the deep electrical structure of the northern segment of the Tan-Lu fault zone, NE China. *Journal of Asian Earth Sciences*, *170*, 118–127. https://doi.org/10.1016/j.jseaes.2018.10.029

Tian, X., Zhang, J., Si, S., Wang, J., Chen, Y., & Zhang, Z. (2011). SKS splitting measurements with horizontal component misalignment. *Geophysical Journal International*, *185*(1), 329–340. https://doi.org/10.1111/j.1365-246x.2011.04936.x

Tian, Y., Ma, J., Liu, C., Feng, X., Liu, T., Zhu, H., et al. (2019). Effects of subduction of the Western Pacific plate on tectonic evolution of Northeast China and geodynamic implications. *Chinese Journal of Geophysics*, *62*(3), 1071–1082.

Wang, H., & Currie, C. A. (2015). Magmatic expressions of continental lithosphere removal. *Journal of Geophysical Research: Solid Earth*, *120*, 7239–7260. https://doi.org/10.1002/2015JB012112

Wang, X., Chen, Q. F., Li, J., & Wei, S. (2016). Seismic sensor misorientation measurement using P-wave particle motion: An application to the NECsaids array. *Seismological Research Letters*, *87*(4), 901–911. https://doi.org/10.1785/0220160005

Wilde, S. A. (2015). Final amalgamation of the central Asian orogenic belt in NE China: Paleo-Asian ocean closure versus paleo-Pacific plate subduction—A review of the evidence. *Tectonophysics*, *662*, 345–362. https://doi.org/10.1016/j.tecto.2015.05.006

Wu, C., Xu, T., Badal, J., Wu, Z., & Teng, J. (2015). Seismic anisotropy across the Kunlun fault and their implications for northward transforming lithospheric deformation in northeastern Tibet. *Tectonophysics*, *659*, 91–101. https://doi.org/10.1016/j.tecto.2015.07.030

Wu, F.-Y., Lin, J.-Q., Wilde, S. A., & Yang, J.-H. (2005). Nature and significance of the Early Cretaceous giant igneous event in eastern China. *Earth and Planetary Science Letters*, *233*(1–2), 103–119. https://doi.org/10.1016/j.epsl.2005.02.019

Wüstefeld, A., Bokelmann, G., Zaroli, C., & Barruol, G. (2008). SplitLab: A shear-wave splitting environment in Matlab. *Computers & Geosciences*, *34*(5), 515–528. https://doi.org/10.1016/j.cageo.2007.08.002

Wüstefeld, A., & Bokelmann, G. t. (2007). Null detection in shear-wave splitting measurements. *Bulletin of the Seismological Society of America*, *97*(4), 1204–1211. https://doi.org/10.1785/0120060190

Xu, M., Li, Y., Hou, H., Wang, C., Gao, R., Wang, H., et al. (2017). Structural characteristics of the Yilan-Yitong and Dunhua-Mishan faults as northern extensions of the Tancheng-Lujiang fault zone: New deep seismic reflection results. *Tectonophysics*, *706*, 35–45. https://doi.org/10.1016/j.tecto.2017.03.018

Xu, Y.-G. (2014). Recycled oceanic crust in the source of 90–40 Ma basalts in North and Northeast China: Evidence, provenance and significance. *Geochimica et Cosmochimica Acta*, *143*, 49–67. https://doi.org/10.1016/j.gca.2014.04.045

Xu, Y.-G., Zhang, H.-H., Qiu, H.-N., Ge, W.-C., & Wu, F.-Y. (2012). Oceanic crust components in continental basalts from Shuangliao, Northeast China: Derived from the mantle transition zone? *Chemical Geology*, *328*, 168–184. https://doi.org/10.1016/j.chemgeo.2012.01.027

Yang, F., Guo, G., Li, J., Chen, Q. F., Chen, Y., & Chen, S. (2022). Panoptic view of mantle flow beneath Trans-continental northeast Asia: Distinct variation detected from~ 2000 km shear wave splitting profile. *Geophysical Research Letters*, *49*, e2021GL097116. https://doi.org/10.1029/2021GL097116

Yang, J., & Faccenda, M. (2020). Intraplate volcanism originating from upwelling hydrous mantle transition zone. *Nature*, *579*(7797), 88–91. https://doi.org/10.1038/s41586-020-2045-y

Yin, A. (2010). Cenozoic tectonic evolution of Asia: A preliminary synthesis. *Tectonophysics*, *488*(1–4), 293–325. https://doi.org/10.1016/j.tecto.2009.06.002

Yu, Y., Gao, S. S., Liu, K. H., & Zhao, D. (2020). Foundered lithospheric segments dropped into the mantle transition zone beneath southern California, USA. *Geology*, *48*(2), 200–204. https://doi.org/10.1130/g46889.1

Zhan, R., & Zhu, G. (2012). Cenozoic activity methods and evolution of the tan-Lu fault zone in Bohai Bay: Evidence from the Qingdong Sag. *Chinese Journal of Geology*, *47*(4), 1130–1150.

Zhang, A., Guo, Z., Afonso, J. C., Handley, H., Dai, H., Yang, Y., & Chen, Y. J. (2022). Lithosphere-asthenosphere interactions beneath northeast China and the origin of its intraplate volcanism. *Geology*, *50*(2), 210–215. https://doi.org/10.1130/g49375.1

Zhang, B., Lei, J., Yuan, X., Zhang, G., He, J., & Xu, Q. (2020). Detailed Moho variations under Northeast China inferred from receiver function analyses and their tectonic implications. *Physics of the Earth and Planetary Interiors*, *300*, 106448. https://doi.org/10.1016/j.pepi.2020.106448

Zhang, M., & Guo, Z. (2016). Origin of Late Cenozoic Abaga-Dalinuoer basalts, eastern China: Implications for a mixed pyroxenite–peridotite source related with deep subduction of the Pacific slab. *Gondwana Research*, *37*, 130–151. https://doi.org/10.1016/j.gr.2016.05.014

Zhang, M., Guo, Z., Cheng, Z., Zhang, L., & Liu, J. (2015). Late Cenozoic intraplate volcanism in Changbai volcanic field, on the border of China and North Korea: Insights into deep subduction of the Pacific slab and intraplate volcanism. *Journal of the Geological Society*, *172*(5), 648–663. https://doi.org/10.1144/jgs2014-080

Zhang, R., Wu, Q., Sun, L., He, J., & Gao, Z. (2014). Crustal and lithospheric structure of Northeast China from S-wave receiver functions. *Earth and Planetary Science Letters*, *401*, 196–205. https://doi.org/10.1016/j.epsl.2014.06.017

Zhang, S., & Karato, S.-I. (1995). Lattice preferred orientation of olivine aggregates deformed in simple shear. *Nature*, *375*(6534), 774–777. https://doi.org/10.1038/375774a0

Zhao, D., Lei, J., & Tang, R. (2004). Origin of the Changbai intraplate volcanism in Northeast China: Evidence from seismic tomography. *Chinese Science Bulletin*, *49*(13), 1401–1408. https://doi.org/10.1360/04wd0125

Zhao, D., Tian, Y., Lei, J., Liu, L., & Zheng, S. (2009). Seismic image and origin of the Changbai intraplate volcano in East Asia: Role of big mantle wedge above the stagnant Pacific slab. *Physics of the Earth and Planetary Interiors*, *173*(3–4), 197–206. https://doi.org/10.1016/j.pepi.2008.11.009

Zheng, S., & Gao, Y. (1994). Azimuthal anisotropy in lithosphere on the Chinese mainland from observations of SKS at CDSN. *Acta Seismological Sinica*, *7*(2), 177–186.

Zheng, T.-Y., He, Y.-M., Yang, J.-H., & Zhao, L. (2015). Seismological constraints on the crustal structures generated by continental rejuvenation in northeastern China. *Scientific Reports*, *5*(1), 1–8. https://doi.org/10.1038/srep14995

Zou, H., Fan, Q., & Yao, Y. (2008). U–Th systematics of dispersed young volcanoes in NE China: Asthenosphere upwelling caused by piling up and upward thickening of stagnant Pacific slab. *Chemical Geology*, *255*(1–2), 134–142. https://doi.org/10.1016/j.chemgeo.2008.06.022